2013

Quasi-steady response of free-to-pivot flat plates in hover

K Granlund
Aerospace Systems Directorate

M Ol
Aerospace Systems Directorate

L Bernal
University of Michigan

Journal of Fluids and Structures 40 (2013) 337–355

Contents lists available at SciVerse ScienceDirect

Journal of Fluids and Structures

journal homepage: www.elsevier.com/locate/jfs

Quasi-steady response of free-to-pivot flat plates in hover

K. Granlund [a], M. Ol [a,*], L. Bernal [b]

[a] U.S. Air Force Research Laboratory, Aerospace Systems Directorate, Wright-Patterson AFB, OH 45433-7542, USA
[b] University of Michigan, Department of Aerospace Engineering, Ann Arbor, MI 48105, USA

ARTICLE INFO

Article history:
Received 2 November 2011
Accepted 23 February 2013
Available online 14 June 2013

Keywords:
Flapping
Leading edge vortex
Pivoting plate
Hover

ABSTRACT

Using force measurements and flow visualization in a water tunnel, we consider motions of rigid flat plates with square edges free to pivot about the leading edge between incidence angles of $\pm 45^{\circ}$. The plate's leading edge undergoes a prescribed periodic rectilinear translation. During most of the translation semi-stroke, the plate rests against its incidence limiter to produce a positive angle of attack; this reverses on the opposite semi-stroke, producing a motion akin to normal-hover with delayed rotation. Three aspect ratios are considered: a nominally 2D, or wall-to-wall plate spanning the tunnel test section, and plates of aspect ratios 3.4 and 5.5. Reynolds number effects in the range of 10 000–31 000 were not found to be significant. Aerodynamic force coefficient history was found to be aspect-ratio invariant, despite difference in flowfield evolution in the wake, and the force coefficients magnitude decreased for decreasing motion amplitudes. Flow visualization gives qualitative evidence for leading-edge and trailing-edge vortices, but no evidence was found of leading edge vortex stability or for contribution of vortices to aerodynamic loads, for sinusoidal or nonsinusoidal imposed motions of the plate. No evidence is found that the vortex system in the wake interacts with the plate during or after semi-stroke reversal. The main operative parameter governing aerodynamic force history is the ratio of semi-stroke amplitude to plate chord. Especially for the larger semi-stroke to chord ratios, aerodynamic response during the translational phase of motion is nearly quasi-steady, with decay in both thrust and force opposing the motion, in proceeding along each semi-stroke. The rotational phase of each semi-stroke is dominated by a loads spike as the plate approaches its incidence limiter. This spike largely disappears when the free-to-pivot plate is replaced with one with a prescribed rotational history. These findings offer favorable implications for analysis of flapping-wings using quasi-steady blade element models.

Published by Elsevier Ltd.

1. Introduction

The classical problem of a rigid flat plate oscillating in two degree of freedom rectilinear motion in an otherwise quiescent fluid remains of both topical applied interest, and of fundamental interest in study of interplay between vortex physics and aerodynamic loads history. We consider the application to abstractions of flapping wings, for either Micro-Air Vehicles (MAVs) or for natural fliers. The two degrees of freedom are translation of the leading edge of the plate, generally but not necessarily sinusoidal; and the pitching of the plate about the leading edge.

* Corresponding author. Tel.: +1 937 232 7761.
E-mail addresses: Michael.Ol@wpafb.af.mil, ol_70@hotmail.com (M. Ol).

0889-9746/$ - see front matter Published by Elsevier Ltd.
http://dx.doi.org/10.1016/j.jfluidstructs.2013.02.020

Nomenclature

a	acceleration-limit parameter, used to define nonsinusoidal translation of plate leading edge
A_s	swept area, $=2bh_0c$
b	plate span
c	plate chord ($=50$ mm)
$C_N(t/T)$	coefficient of normal force, in direction of translation of plate leading edge, $=N/(0.5U_{ref}^2bc)$
$C_T(t/T)$	coefficient of thrust, perpendicular to direction of translation of plate leading edge, $=T'/(0.5U_{ref}^2bc)$
C_p	power coefficient, $=P/(0.5U_{ref}^3bc)$
f	motion frequency
$G(t/T)$	function used to smooth acceleration discontinuities in nonsinusoidal translation of plate leading edge
$h(t/T)$	plate leading edge translation as a function of time
h_0	nondimensional translation amplitude, $=h/c$
M	Figure of Merit: ratio of ideal power to actual power for producing a given stroke-averaged thrust
$N(t/T)$	normal force. Component of the force in the direction of the leading edge motion
Re	Reynolds number, $=U_{ref}\,c/\nu$
T	motion period, $=1/f$
$T'(t/T)$	thrust; component of the force normal to the direction of the leading edge translation
$\overline{T}$	stroke-averaged thrust
t/T	phase of plate leading edge imposed motion, $0\le t/T\le 1$
U_{ref}	reference speed; maximum translation speed of the plate's leading edge, $=2\pi fh_0c$
$\theta(t/T)$	plate incidence angle as a function of time, relative to direction of leading-edge translation

A significant challenge for flapping-wing MAVs, especially in hover, is to achieve flight control authority through modulation of wing kinematics, without relying on a conventional fixed-wing empennage. Considerations of weight and mechanical complexity generally mean minimizing the actuated degrees of freedom by relying on passive wing deflections throughout the flapping stroke history. Doman et al. (2010) proposed a flight control scheme for the flapping-wing prototype developed by Wood (2007), where the wing leading edge is directly actuated in a sweeping motion, but the wing incidence angle is free to float between limiters, as a balance between the inertia of the wing (and of the ambient fluid) and the motion-induced dynamic pressure. The incidence angle is generally at the limiter throughout the "translation" phase of each semi-stroke, with a rapid rotation from one limiter side to the other, near the extremum of each semi-stroke. Doman et al. (2010) assume a quasi-steady lift coefficient time history throughout the translation stroke, using the sectional lift and drag relations developed by Dickson and Dickinson (2001) to calculate lift (thrust) and resistive force (here termed normal force), assuming a non-lifting rotational phase. The former assumption is probably justified for conceptual-design purposes based on results for sinusoidal periodic plunge for moderate Strouhal number by Ol et al. (2009), where one finds remarkable robustness of the simple $C_L=2\pi\alpha$ even for large incidence angles and high motion rates, whether or not a leading edge vortex is present. But the latter assumption is only valid if the stroke fraction occupied by the rotation is small, and post-rotation transients dissipate quickly. And since the incidence angle time history during rotation is passively accepted from the combination of body dynamics (wing mass and moment of inertia, hinge dynamics, etc.) and aerodynamic loads (time history of pressure distribution on the wing), the actual incidence angle history is not known a priori.

We also aim to connect the fairly broad literature on "normal hover" for imposed translation and rotation time history by Freymuth (1990), with a rectilinear version of the motion assumed by Doman et al. (2010). Sane and Dickinson (2001) found that constraining the pitch angle between $\pm 45^\circ$ maximizes lift production, and this value is also used in the analysis by Doman et al. (2010). Hinging about the leading edge, as opposed to some other chordwise location was found by Dickinson et al. (1999) to be maximally favorable for thrust production. Kurtulus et al. (2006), Milano and Gharib (2005) and Trizila et al. (2011) have studied varying the relation between rotational and translational kinematics to maximize thrust production, which results in more elaborate motion kinematics than the motion assumed by Doman et al. (2010). The more general problem of a hinged plate with a torsional spring, or multiple links connected by torsional springs, was considered in recent 2D computations by Eldredge (2007) and Vanella et al. (2009). Computationally, one can arrive at optimal combinations of hinge stiffness and damping, plate masses and moments of inertia, such that the combined flapping motion maximizes thrust production, propulsion efficiency, or some other desired parameter.

DeVoria and Ringuette (2012), Jones and Babinsky (2010), Letink and Dickinson (2009), Visbal et al. (2013) and Yilmaz et al. (2010) have documented the importance of the leading edge vortex (LEV) in aerodynamic force production, both in translational and flapping motions and including three-dimensional effects. Jones and Babinsky (2011) offer the suggestion that acceleration of the plate leading edge may promote LEV formation and stability, and inversely, a sharp acceleration of the leading edge followed by a long run of steady translational speed may lead to early LEV detachment. An important question is to what extent intra-cycle velocity and acceleration history of flapping wings in hover affects the aerodynamic force generation history—namely, how this history departs from quasi-steady response. Other important questions include how such force production correlates with LEV formation and stability, the roles of plate aspect ratio and Reynolds number.

In the present work we study experimentally the aerodynamics of free-to-pivot flat plates in translational motion in quiescent fluid. Using the speed and power of a large electric motion rig operating above a free-surface water tunnel, we study passive pitch change across $\pm 45^\circ$ rotation of the plate about its leading edge, with prescribed sinusoidal and nonsinusoidal periodic translation of the leading edge. We vary Reynolds number, translational amplitude and plate aspect ratio, accepting the plate's rotational history from the passive rigid body dynamics, and measure the aerodynamic force on the plate. Using dye and laser fluorescence flow visualization we examine the flow evolution to determine the role of LEV and other vortical flow features on force generation. We seek to determine to what extent aerodynamic force production is quasi-steady with respect to history of the plate's incidence angle. Furthermore we investigate non-steady effects by comparing force histories for sinusoidal imposed motion of the plate's leading edge, with that of motions where the leading edge is accelerated over a small duty cycle, followed by constant-speed translation to determine the effects of intra-cycle motion kinematics on force production. Also the relative importance for aerodynamic force production of the rotational phase of motion vs. the translational phase, and whether there is an optimal ratio of semi-stroke to chord ratio for aerodynamic thrust efficiency. To further understand the physics of plate rotation, we compare the free-to-pivot case with a kinematically equivalent motion where both plate translation and rotation are imposed.

2. Experimental methods

2.1. Facility and motion mechanism

The U.S. Air Force Research Laboratory's (AFRL) Horizontal Free-surface Water Tunnel is fitted with a three degree of freedom electric rig enabling independent control of pitch or rotation, plunge or heave, and surge or streamwise-aligned translation. In the present study, the tunnel is operated as a towing tank, with the rig providing the model motions. Photographs of the tunnel and model installation, and schematic of the three models are shown in Fig. 1. The motion rig consists of three linear motors; two are mounted vertically above the tunnel's free-surface on a carriage riding on rails, while the third is mounted horizontally, moving the carriage in the surge direction. The two vertical motors each actuate a rod, connecting to a coupler piece housing the load cell (middle portion of Fig. 1) achieving independent combination of pitching and plunging motion. The three motors are controlled via a Galil DMC-4040 motion controller from pre-programmed motion scripts achieving <0.1 mm linear- and $<0.2^\circ$ angular position error. For free-to-pivot plates, only the third motor (surge motion) is used, but all three motors are used to execute imposed rotation/translation motions. More detail on the tunnel and rig operation is given in Ol et al. (2009).

To better isolate the model from the rig, the plates are hung from a streamlined strut cantilevered in front of the load cell. The 2D plate is wall-to-wall with 1.0 mm gap on each tip, 5 cm chord, 6% thickness and rectangular edges. The same mounting procedure and motion control is used for the AR = 3.4 and 5.5 plates. The test section floor is ~6 chords below the plate trailing edge. Each of the models is hinged at the midspan of its leading edge, and constrained in rotation by mechanical limiters (hard plastic stops) in the vertical strut holding the leading-edge pivot assembly. Each period of motion is subdivided into two semi-strokes, with semi-strokes bounded by endpoints in the translation of the leading edge. As its support is translated, pressure difference between the advancing and retreating side of the plate forces the plate to rotate towards its retreating pitch limiter, until reaching the nominally 45° incidence angle limit. This is the "rotational phase" of motion, occurring towards the beginning of each semi-stroke. The plate remains at 45° incidence until roughly the final 10–20% of each semi-stroke, before beginning the rotational phase anew. In the following, the "translational phase" of each semi-stroke is taken to mean that range of t/T during which the plate's incidence angle is nominally constant. For the case of imposed rotations, the leading edge hinge is fused, and rotation is imparted through action of the three linear motors.

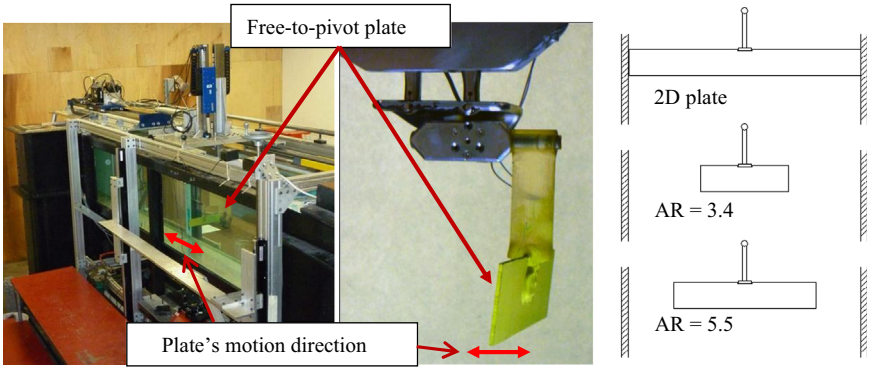

Fig. 1. Experimental installation. Test section and motion apparatus mounted above test section of the AFRL Horizontal Free-surface Water Tunnel (left); wall-to-wall plate at rest (middle) and schematic of the three plates, upstream view (right). The plate's motion direction and location in the left and middle photographs are as labelled.

2.2. Flow visualization and force measurement

Flowfield measurements are limited here to qualitative inferences from dye injection with planar laser fluorescence. Stainless steel lines with 0.5 mm internal diameter were glued to the model surface at the 3/4 span location at the leading and trailing edge, firing outboard along each respective edge. The dye is a high concentration water solution of Rhodamine 6G, illuminated by a ~2 mm-thick laser light sheet (524 nm wavelength) positioned normal to the span direction approximately 1 mm outboard of the dye tube exits. Images were recorded with a PCO Dimax high speed camera operated at 50 frames per second, with the camera and laser synchronized using an external pulse source, and grayscale values inverted to render high concentrations of dye black, in an otherwise white background. The advantage of planar laser illumination over conventional food-coloring dye injection in white-light is that the former limits the region of regard essentially to the plane of the laser light sheet. This is useful for problems with strong out-of-plane flow, effectively diffusing and dissipating the dye streak. Imaging limited to dye fluorescence in the plane of interest in principle allows for more incisive regard of flowfield regions identified with leading-edge and trailing-edge vortices.

Flow visualization is also used to measure the angular position history of the plate as it rotated between its incidence limiters. Measurement uncertainty of the free-to-pivot plate incidence angle is $\pm 1.5^\circ$, owing to elasticity of the plastic hinge limiters; in contrast, uncertainty in incidence angle for the fused-hinge plate is estimated as $\pm 0.5^\circ$.

Force measurements were obtained with an ATI Nano25 IP68 6-component sensor, oriented to align its maximally sensitive channels with the in-plane motion forces. This orientation also has the advantage of reducing the sensitivity of the sensor to hydrostatic pressure bias since the free-to-pivot motions are performed at constant depth.

2.3. Data reduction procedure

Force data is sampled at 100 Hz for motions < 0.5 Hz, and 1000 Hz for motions > 0.5 Hz. Data is low-pass filtered at 73 Hz in the ATI NetBox interface, and transferred via Ethernet to the host computer. Force data is triggered externally via a pulse from the DMC-4040 controller at motion onset, and is later merged with motion data, to obtain synchronization of $C_T(t/T)$ and $C_N(t/T)$ with $h(t/T)$ and $\theta(t/T)$. All motions are repeated for 20 cycles, and before storing the data in the host computer for further processing, the sensor calibration is applied and measured forces in the load cell frame of reference are converted to the plate-relevant coordinate system.

Post-processing of data is implemented in Matlab, and consists of a low-pass filter step, phase averaging step and tare removal step. The low-pass filter is a zero-phase two-pass 4th order Chebychev II filter with cutoff frequency 50x the motion frequency. Wang et al. (2004) report attainment of periodicity in force-history after the first two periods after motion onset. Birch and Dickinson (2003) reported no difference in force between the first and fourth return stroke, but did observe flow field differences. With that motivation, in the phase average step of data analysis, the first three cycles of each sequence are discarded from the calculation of the cycle mean and variance. For tare removal for the freely-hinged plate, the product of the mass of the plate and its mount, and the imposed acceleration of the plate's mount, is removed from the force measurements. Since the density of the plate is close to the fluid density and the total mass of the plate itself is an order of magnitude smaller than the added mass, no attempt is made to subtract inertial effects of the plate's rotation from the total force measurement. For the case where the plate's leading edge hinge is fused, and both rotation and translation are prescribed, a dynamic tare is performed with the same model and a point-mass that replaces the plate. The point-mass is equal to the plate's mass and is placed at the location of the plate's center of mass.

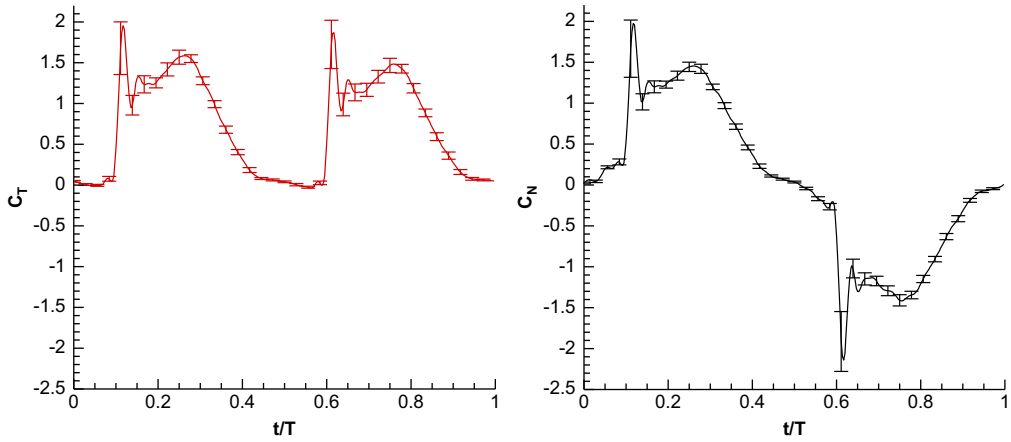

Fig. 2. Thrust coefficient (left) and normal-force coefficient (right) with error bars at 95% confidence intervals for a representative case: AR = 5.5 freely-hinged plate, semi-stroke to chord ratio of 3.1, frequency of 0.532 Hz. An error bar is plotted for every 10th data point.

Table 1
Aspect ratio study (2D, AR=3.4 and AR=5.5), sinusoidal LE motion of free-to-pivot plates. Amplitudes of semi-stroke to chord ratio are in columns, and physical frequency of LE motion (Hz) are in rows. Nominal Reynolds number (left column) is proportional to product of frequency and semi-stroke amplitude. Every entry represents a run for each of the three plates.

Frequency	Amplitude of semi-stroke to chord ratio				
Nominal Re	6.20	3.10	1.55	0.775	0.3875
10000	0.155	0.211	0.422	0.844	1.688
13000		0.316			2.128
20000	0.211	0.422	0.844	1.688	
26000		0.532	1.064		
31500	0.335				

Table 2
Motion profile study of the AR=5.5 plate, comparison of sinusoidal imposed LE motion, $a=2$ and $a=3$.

Frequency	Amplitude of semi-stroke to chord ratio		
Nominal Re	6.20	3.10	1.55
10 000	0.1055	0.211	0.422
20 000	0.211	0.422	0.844

Force data are non-dimensionalized by the plate's planform area and either instantaneous- or maximum leading edge translation velocity. Time is non-dimensionalized by motion period; that is, t/T runs from 0 to 1. Representative force-data error analysis, plotting the 95% confidence intervals as error bars for coefficients of thrust and normal-force, is given in Fig. 2. The 95% confidence interval is based on the computed sample variance and sample size (17 cycles). Normal-force coefficient history qualitatively resembles a sinusoid with extremum at approximately the midpoint of each semi-stroke, punctuated by a strong force spike at $t/T\sim0.12$ and 0.62. The normal force is generally in the direction opposite to the motion, and therefore changes sign with the direction of plate translation. Thrust coefficient resembles a rectified sine wave with similar spikes at $t/T\sim0.12$ and 0.62, since thrust is positive on both fore and aft semi-stroke. Measurement uncertainty is greatest during the force spike, and is otherwise typically less than 0.2 in coefficient form, which corresponds to much less than the load cell manufacturer's quoted calibration tolerance of 1% of full metric range.

2.4. Test matrix

The principal parameter is the ratio of semi-stroke amplitude to plate chord. Values of 6.2, 3.1, 1.55, 0.775 and 0.3875 are considered in this study. The peak-to-peak semi-stroke is twice the amplitude, and therefore varied from 12.4 to 0.775 chords. In what follows, "semi-stroke to chord ratio" refers to the single-sided amplitude. All three plates (nominally 2D, AR=5.5 and AR=3.4) were subjected to the motions in Table 1, while only the AR=5.5 plate was used for the non-sinusoidal motions in Table 2. Comparison between prescribed-rotation and free-hinge dynamics was limited to the AR=5.5 plate for a semi-stroke to chord ratio of 3.1.

The choice of semi-stroke to chord ratio of 3.1 was motivated by comparison with the flapping-wing arrangement of Doman et al. (2010), where the wing flapped through an arc length of approximately $\pm3.1c$ at its radius of gyration. The need to have sufficient motion-induced dynamic pressure to swing the plate against its incidence-angle limiters determines the lower bound of plate leading-edge oscillation frequency, while the upper-bound stems from the rig overheating if running a large number of periods at high oscillatory speeds. Larger or smaller stroke amplitudes allow one to compare the extent of quasi-steady response over a range of translation lengths, or equivalently, convective times.

3. Results

We first consider the aerodynamic force histories and flowfield visualization of the three plates, to assess the role of aspect ratio and Reynolds number. Next, we focus on the extent to which the force data is quasi-steady during the translational portion of each semi-stroke, and then assess the role of forces in the rotational phase of motion. We compare the free-to-pivot plate and the case of prescribed rotation, and assess thrust efficiency and thrust production as a function of stroke amplitude for the various cases.

3.1. Force generation by free-to-pivot plates

The aerodynamic force coefficients $C_T(t/T)$ and $C_N(t/T)$ are plotted together with the plate's incidence history, $\theta(t/T)$, in Fig. 3. The plate's incidence angle is negative at time $t/T=0$, and does not pass through the line of symmetry (that is,

0° incidence) until some positive t/T. All cases except for the 6.2c 0.1055 Hz case can therefore be regarded as "delayed rotation" (Wang et al., 2004). The exceptional case, which is of largest amplitude and smallest frequency considered here, has slightly advanced rotation, since $\theta > 0^\circ$ at $t/T=0$. Curiously, there is no obvious difference in aerodynamic force coefficient history between the one advanced-rotation case and the remaining cases, with the exception of the absence of "spikes" in C_T and C_N histories. In particular, there is no secondary peak in thrust coefficient, often attributed to wake-capture effects (Dickson and Dickinson, 2001).

In Fig. 3(a) through (d), the history of the plate's incidence angle, $\theta(t/T)$, can be segregated in each semi-stroke into two parts: a long run of nearly constant $\theta(t/T)$, termed "translational", where the plate is resting against its incidence-limiter; and a fairly abrupt period of rotation, where $\theta(t/T)$ varies from one extreme to the opposite extreme in passing to the succeeding semi-stroke. The plate's incidence-history resembles the effective angle of attack history in thunniform swimming, identified by Schouveilier et al. (2005).

The aerodynamic force histories in Fig. 3 are rife with "spikes" in magnitude of thrust and normal force, of duration $\sim 0.05t/T$ or less, generally centered around the t/T value where the plate reaches its incidence limiter. These spikes suggest noncirculatory aerodynamic force, associated with a volume of fluid accelerated together with the rotational acceleration of the plate. The mass times acceleration of a reference volume of fluid contributes to the aerodynamic load on the plate. In Fig. 3, in every case that the limiter-strike event occurs, a spike in normal force and thrust coefficient follows. Fig. 3(a) and (f) have no limiter strike event. Fig. 3(a) is 6.2c amplitude and 0.1055 Hz frequency, where the dynamic pressure from the plate's motion is low and the plate is brought against its incidence limiter only gradually. Fig. 3(f) has 0.3875c amplitude; for all 0.3875c cases, regardless of frequency, the plate never reaches its incidence limiter at all, and its motion is best described as a continuous rotation about the plate's midchord. The 0.3875c case therefore has a completely smooth response in thrust and normal force.

The short duration of the loads-spikes, $\sim 0.05t/T$, is evidently too brief to be ascribable to a vortex-related event. Flowfield evolution snapshots in Figs. 5 and 6, which will be discussed in more detailed below in Section 2, are spaced by $t/T=0.083$, and over this increment, the flow pattern evolves fairly slowly. The rotational portion of each semi-stroke occupies a duration of $t/T\sim 0.12$–0.18, which is considerably longer than the duration of the loads spike. It is therefore unlikely that these spikes are due to "rotational lift" (Sane and Dickinson, 2002), or in other-words, the pitch-rate effect in unsteady airfoil theory (Ol et al., 2009). What is more likely is that during most of the rotational portion of each semi-stroke, kinetic energy of the rotating plate is balanced by energy of the consequently accelerating ambient fluid. This, in fact, determines the rotational history of the freely-pivoting plate. But when this plate reaches its incidence limiter, such balance is no longer possible, and a loads-spike results.

Unfortunately there is insufficient accuracy in the trace of the plate's incidence-angle history to conclude definitively whether the force spikes are due to noncirculatory loads or to mechanical impact between the plate and its plastic limiter. We will revisit this question below in section 5, where we consider the effect of non-sinusoidal translation motion kinematics, and in section 6 for the fused-hinge plate, which has no incidence limiter-impact event.

3.2. Aspect ratio and Reynolds number independence

If aerodynamic loads, normalized by the plate's planform area, collapse to the same coefficient for the same imposed history of the plate's leading edge, then this suggests (1) aspect ratio independence, and (2) repeatable behavior of the hinging mechanism and plate rigid-body dynamics across the three aspect ratios. This is indeed found to be the case in Fig. 4, which compares the three aspect ratios across a range of semi-stroke to chord ratio and two different values of the Reynolds number. Reynolds number based on peak translational speed of the leading edge is 20 000 in Figs. 4(a)–(d), and 10 000 in Fig. 4(e)–(f).

That the aspect ratio plays such little role in affecting thrust production or the resistive force accompanying the plate's motion, is both a convenience and a source of consternation. It is a convenience because it appears to vindicate application of blade-element theory to flapping-wing aerodynamics, where one is concerned only with the two-dimensional (sectional) properties of the wing – the chord, camber, angle of attack and so forth – and integrates across the wing span, without regard to tip vortices or spanwise variation in downwash distribution. But aspect ratio independence is also a source of consternation, because it suggests that neither spanwise flow (with its putative role in leading edge vortex stabilization), nor spanwise pressure gradients due to tip vortices, have significant effect on aerodynamic performance. Also, blockage in the water tunnel test section, on account of a possible recirculating flow set up by the plate's motion, seems to be independent of both aspect ratio and plate area.

The one exception to independence of force coefficients on aspect ratio is that of the 2D plate for the motions of 3.1c semi-stroke amplitude. On the fore semi-stroke, all three plates evince similar behavior, but on the return semi-stroke, the 2D plate shows a maximum force after the spike at an earlier phase than the other cases. The lack of symmetry between the fore and return strokes in this case is likely due to a slight misalignment of the plate or greater wobbling of the 2D plate about its hinge, which is plausible because this is the heaviest plate with the largest spanwise-direction moment of inertia.

We next turn to flow visualization. Fig. 5 examines aspect ratio independence from the viewpoint of flow visualization for the three plates, for the semi-stroke to chord ratio of 3.1, focusing on events at the conclusion of one semi-stroke ($t/T\sim 0.875$–1) and the beginning of the next semi-stroke ($t/T\sim 0$–0.2). Fig. 6 considers the semi-stroke to chord ratio of 1.55; both figures are at $\mathrm{Re}=10\,000$.

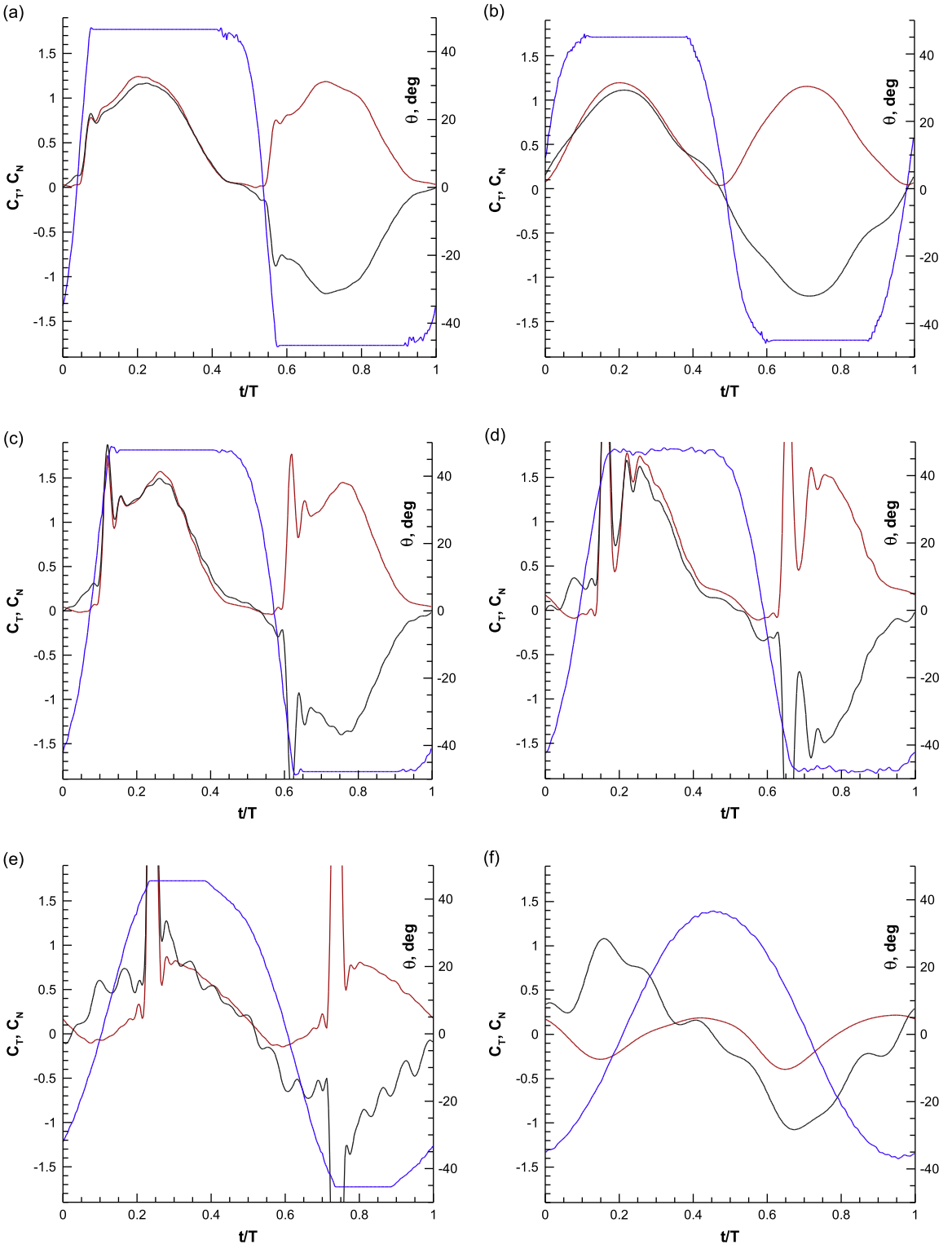

Fig. 3. Thrust coefficient (red), normal-force coefficient (black) and incidence angle (blue) histories for semi-stroke to chord ratios of 6.2 (a, b), 3.1 (c), 1.55 (d), 0.775 (e) and 0.3875 (f). The 6.2-chord case is shown for the highest and lowest motion frequency, 0.335 Hz (a) and 0.1055 Hz (b), since case (b) is the only case where rotation is not delayed with respect to translation. Case (c) has frequency 0.422 Hz, (d) and (e) are 0.844 Hz, and (f) is 1.688 Hz. Reynolds numbers are 20 000 in (a) through (d) and 10 000 in (e) and (f). (For interpretation of the references to color in this figure legend, the reader is referred to the web version of this article.)

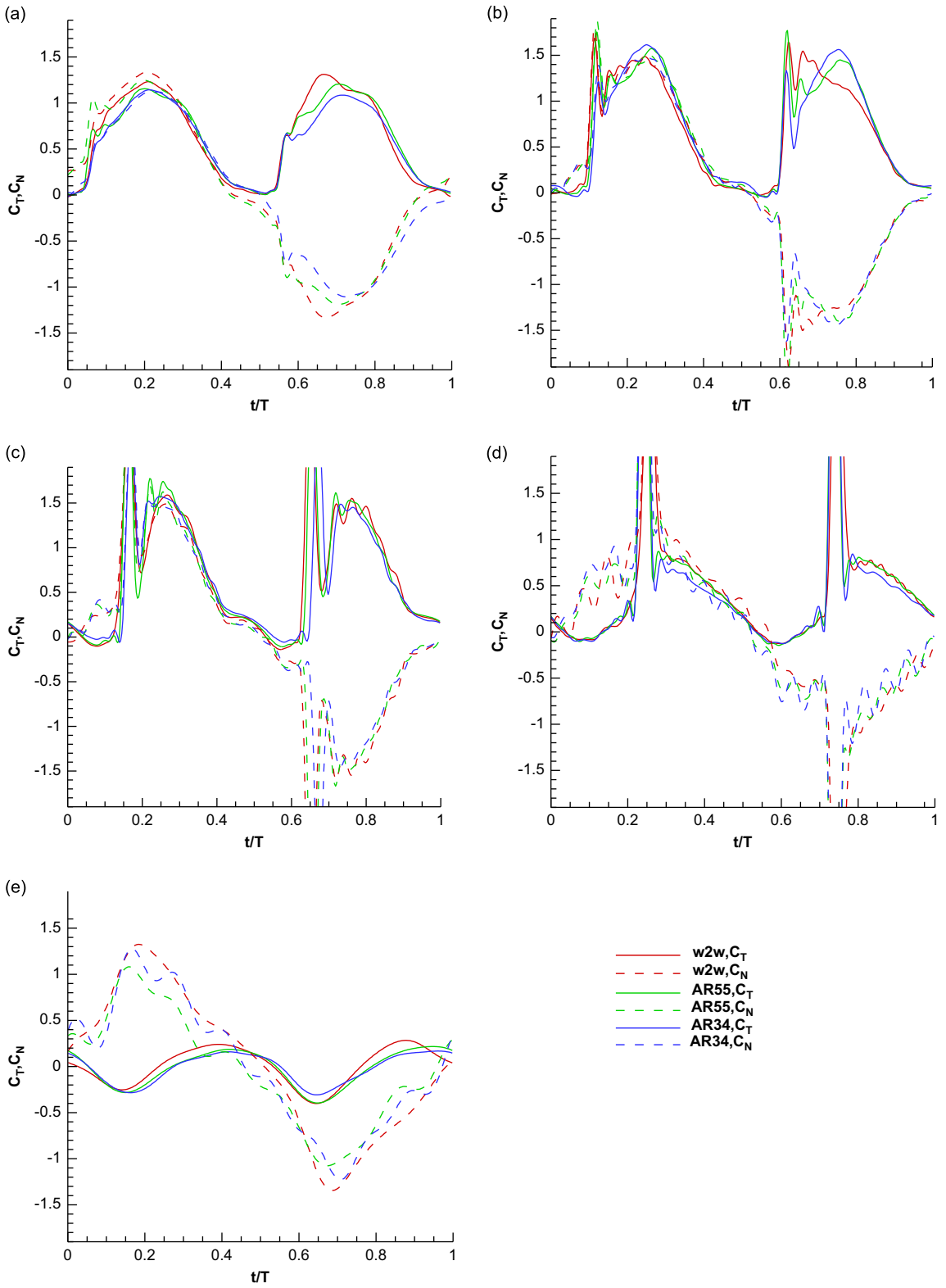

Fig. 4. Parameter study of plate aspect ratio showing thrust coefficient (solid curve) and normal force coefficient (dashed curve) for the 2D or wall-to-wall plate, and plates of aspect ratio 5.5 and 3.4. (a) $h_0=6.2$, $f=0.211$ Hz, Re=20 000; (b) $h_0=3.1$, $f=0.422$ Hz, Re 20 000; (c) $h_0=1.55$, $f=0.844$ Hz, Re=20 000; (d) $h_0=0.755$, $f=0.844$ Hz, Re=10 000; and $h_0=0.3875$, $f=1.688$ Hz, Re=10 000.

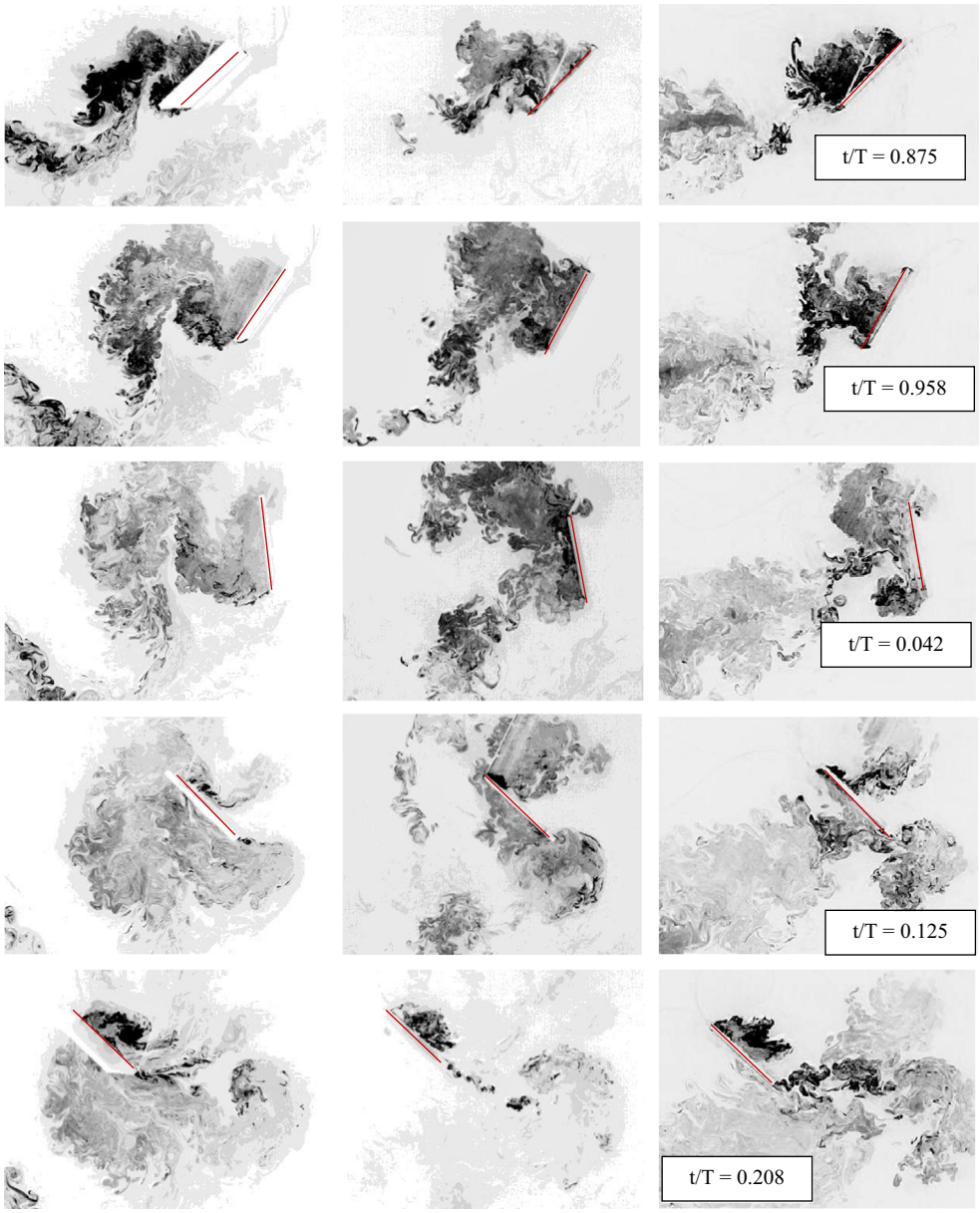

Fig. 5. Flow visualization by laser fluorescence of Rhodamine dye for the 2D plate (left column) and plates of aspect ratio 5.5 (middle column) and 3.4 (right column). Semi-stroke to chord ratio of 3.1. Phases of motion, from top row to bottom: t/T=0.875, 0.958, 0.042, 0.125, and 0.208 (that is, in increments of 30° of motion phase). Intersection of light sheet with plate is marked by red line segment. (For interpretation of the references to color in this figure legend, the reader is referred to the web version of this article.)

A flow structure resembling an LEV appears in Fig. 5 a t/T~0.125; in Fig. 6 its appearance is delayed until t/T~0.2, or in other words, later in the translational portion of semi-stroke when normalized by time, but at approximately the same translational displacement when normalized by chord. Noting that one should not conflate dye concentration with evolution of vorticity, but using dye concentration as a qualitative surrogate for LEV size and growth, one finds that this "LEV" grows during the translational phase of each semi-stroke, and then convects downstream chordwise along the plate, in the plate's reference frame. For the 3.1c motion, the LEV eventually grows to cover the entire suction-side of the plate, with broadening and diffusion of the dye streak suggesting LEV shedding. For the 1.55c motion, there is insufficient translational stroke length for the LEV to cover the entire suction-side of the plate, and LEV growth is finally terminated as the plate's leading edge decelerates and rotation commences, towards the end of each semi-stroke. In no case is there evidence of interaction of the plate with the vortex system produced in the previous semi-stroke; that is, from qualitative flowfield observations, there is no wake-capture effect.

In Fig. 6, the LEV formed in the nth semi-stroke persists into the beginning of the $n+1$th semi-stroke (t/T~0.042) and "wraps around" the plate's leading edge as the plate continues to rotate (t/T~0.125). This "wrapping" is evidently

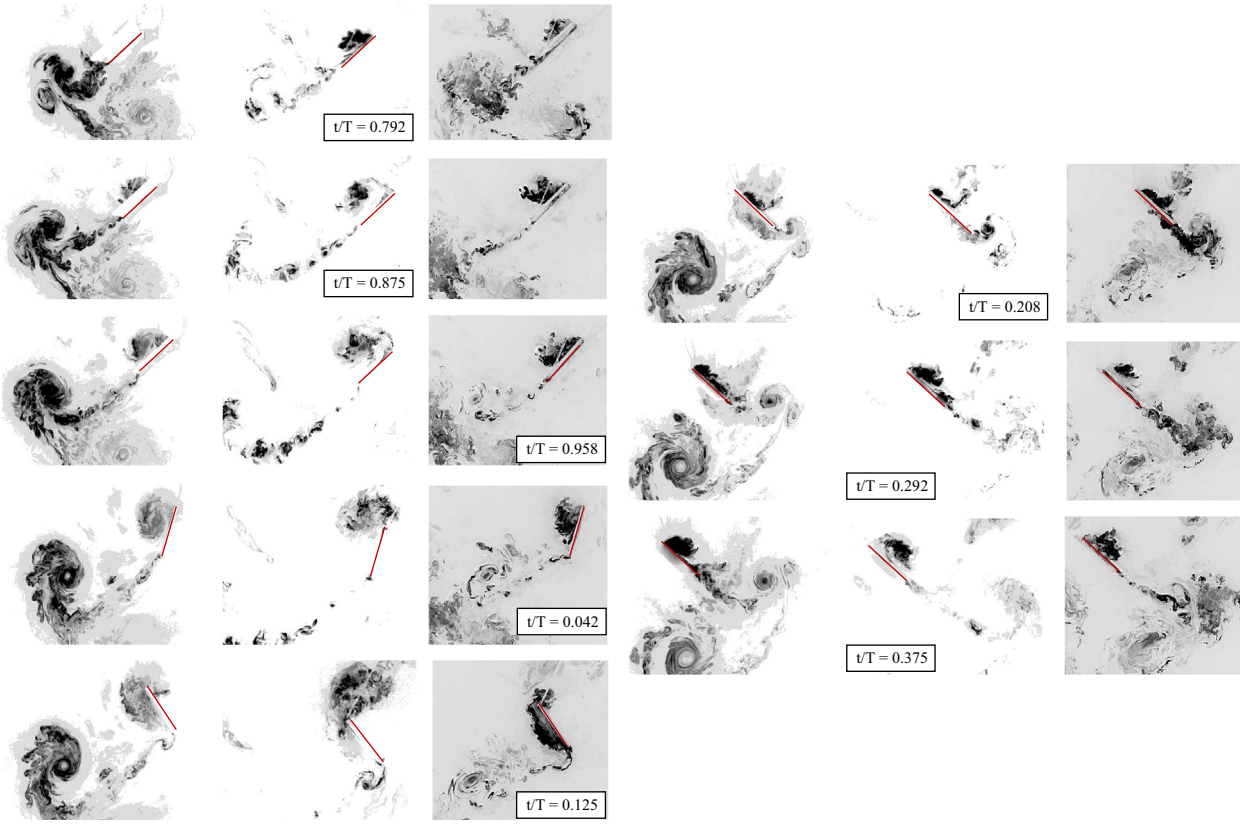

Fig. 6. Flow visualization by laser fluorescence of Rhodamine dye for the 2D plate (left column) and plates of aspect ratio 5.5 (middle column) and 3.4 (right column). Semi-stroke to chord ratio of 1.55. Phases of motion, from top row to bottom: t/T=0.792, 0.875, 0.958, 0.042, 0.125, 0.208, 0.292 and 0.375 (in increments of 30° of motion phase). Intersection of light sheet with plate is marked by red line segment. (For interpretation of the references to color in this figure legend, the reader is referred to the web version of this article.)

aspect-ratio dependent, as the apparent size and placement of the LEV in Fig. 6 at t/T~0.125 differs between the three aspect ratios. But for all three plates, the nth-semi-stroke LEV is ejected between t/T~0.125 and 0.208, and a new LEV forms. The trailing edge vortex system is more difficult to visualize, as evidently local pressure gradients are lower at the trailing edge than at the leading edge, and dye entrainment is less vigorous. Nevertheless, in Fig. 6 at t/T~0.208 one observes a pair of vortices near the trailing edge, formed during the plate's rotation. It is the subsequent evolution of this vortex pair that is the principal difference in flowfields between the three plates. For the nominally 2D plate, a strong trailing vortex system is clearly visible in Fig. 6, forming a vortex street associable with a “jet” of net vertical momentum flux necessary to account for the plate's lift. For the AR=5.5 and 3.4 plates, such a vortex system is difficult to discern, perhaps because of stronger spanwise flow and the resulting flowfield complexity. In Fig. 5 there is no evidence for such vortex street for any of the plates, whence we conclude that for the 3.1c motion amplitude the flowfield is more aspect-ratio-independent than it is for the 1.55c amplitude. Even though dye diffusion precludes the rendering of a definitive conclusion, one can observe that in all cases the vortex system convects downward in the reference frame of the plate, bespeaking a net momentum flux and therefore a positive lift.

As will be seen in discussions below, this “jet” is qualitatively apposite with higher thrust production in the lower-amplitude cases, provided that the motion amplitude is still large enough to force the plate to attain its incidence angle limiters. The greater coherence of vortices, both leading-edge and trailing-edge, with decreasing semi-stroke amplitude, suggests that vortex stability can be related to a formation-time by Milano and Gharib (2005), though we do not speculate here on the most appropriate definition of such a time scale, or its optimum value. But intuitively, a shorter semi-stroke leaves less time for vortices to develop and therefore to shed. A shorter semi-stroke does not, however, directly account for why a stronger vortex would form in the first place.

There is no obvious connection between any of the evinced flow field structures in Figs. 5 or 6, with the respective force histories in Fig. 4. More precisely, there is no local extremum in the force histories in Fig. 4 which one might ascribe to vortex formation or shedding. This suggests that the aerodynamic response ought to be quasi-steady. Here it is perhaps again worth noting the distinction between delayed-rotation and advanced-rotation. Sane and Dickinson (2002) also found that energy from the shed leading edge vortex can be recovered through wake capture only when the plate's rotational phase is advanced relative to the translation. This is consistent with the apparent relative unimportance of the LEV in the present case, which is effectively that of delayed rotation. Lastly, we note that neither for the 3.1c nor the 1.55c motion does

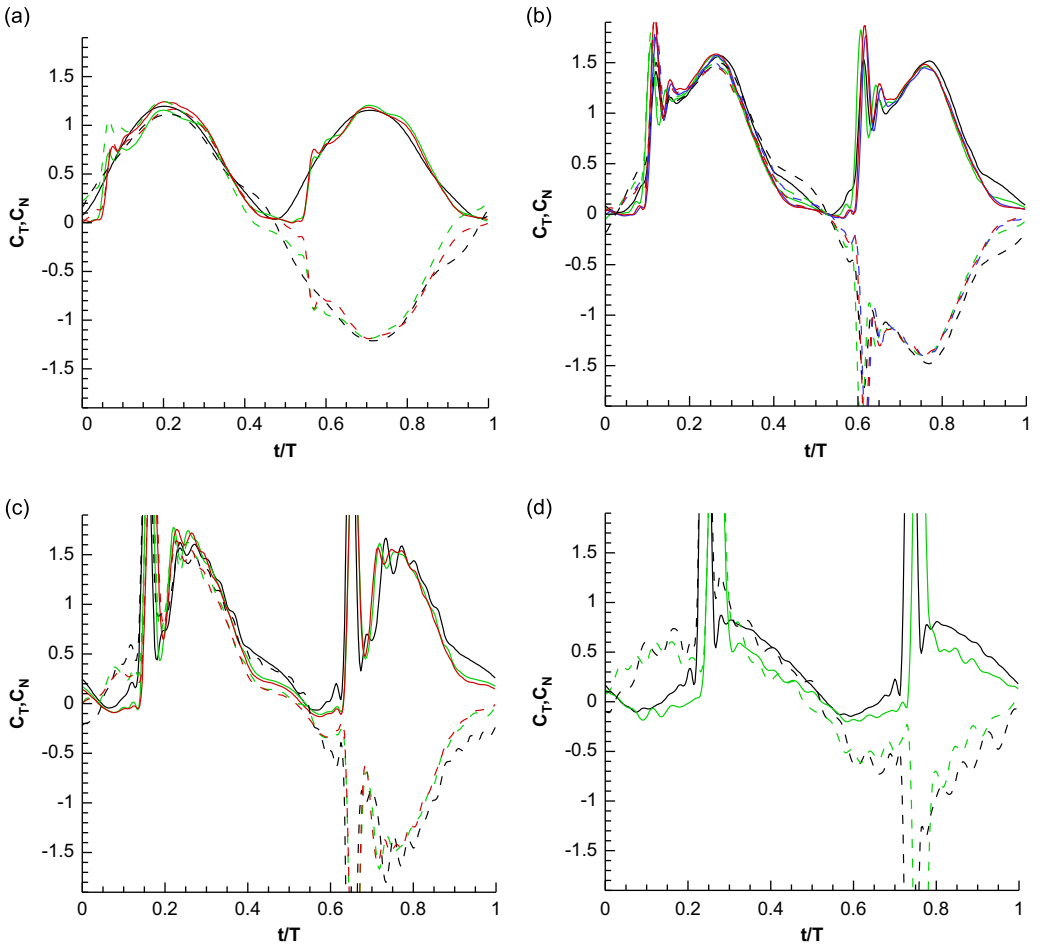

Fig. 7. Parameter study of Reynolds number dependency for the aspect ratio 5.5 plate. C_T solid lines, C_N broken lines. (a) $h_0=6.2$, black Re=10 000; green Re=20 000; red Re=31 500. (b) $h_0=3.1$, black Re=10 000; green Re=13 000; blue Re=20 000; red Re=26 000. (c) $h_0=1.55$, black Re=10 000; green Re=20 000; red Re=26 000. (d) $h_0=0.775$, black Re=10 000; green Re=20 000. (For interpretation of the references to color in this figure legend, the reader is referred to the web version of this article.)

plate aspect ratio appears to affect LEV stability or growth. This is consistent with aspect ratio independence of both thrust and normal-force.

One expects three-dimensional complexity in LEV evolution for a finite aspect ratio plate accelerating in a steady free-stream, as observed for example by Visbal et al. (2013) for plunging and Yilmaz et al. (2010) for pitching and plunging. In the present case, there is no free stream in the lab-frame. Although sectional slices along the 3/4 spanwise station in Figs. 5 and 6 do not evince an interaction between the putative LEV and a tip-vortex structure, presumably a lifting plate of finite aspect ratio does have tip vortex interaction, and this interaction affects LEV evolution. But to reiterate, such interaction, however it affects the flowfield, does not cause a marked aspect-ratio effect on aerodynamic force production.

We next consider Reynolds number effects on the aerodynamic force coefficients. Because both Reynolds number and the aerodynamic coefficients are defined with respect to the plate's leading edge's speed, some care is required in interpreting putative Re-effects. If the dynamic pressure due to the plate's imposed leading-edge motion is too low, there will be insufficient force to rotate a plate of a given mass and moment of inertia against its pitch incidence limiter. So as leading edge speed is reduced, not only is Reynolds number reduced, but also the plate's kinematics is altered. Conversely, when the plate's leading edge speed is increased beyond some threshold, Reynolds number also increases, but the plate's rotational kinematics no longer vary with speed. So in the latter eventuality, any change in aerodynamic coefficients with higher plate leading edge speed is quite directly a Reynolds number effect, whereas in the former, the reason for different aerodynamic coefficients at lower speeds may simply be from a difference in rotational kinematics.

The parameter study in Fig. 7 evinces no Reynolds number dependency over the observed Re range. The exception is the 6.2*c* case at 0.1055 Hz frequency (see Fig. 3), where the slow rotation of the plate results in too gentle of an approach against the pitch limiter to produce a force spike. An increase in frequency, and dynamic pressure, produces a more pronounced force spike, but this instantaneous event has seemingly no effect on the force generation during the rest of the cycle.

3.3. Quasi-steady force approximation to the translational motion

Fig. 8 shows an alternative normalization of normal- and thrust-coefficients, using the instantaneous translation velocity of the plate's leading edge (LE) throughout the cycle, instead of the maximum LE translation velocity. At the translation extrema of $t/T=[0, 0.5, 1]$ where the LE speed is zero, the force coefficients under such normalization approach infinity because of division by zero. But as LE speed increases going into each semi-stroke, normalization by instantaneous plate-LE speed yields more insight into the extent to which the aerodynamic response may be quasi-steady.

We focus on the translational portion of the fore semi-stroke, which is the portion of time after the plate has reached its incidence limiter but before it has commenced rotation away from its incidence limiter, towards the end of the fore semi-stroke. By supposition, the plate's incidence angle is constant throughout this time. If the aerodynamic response were to be truly quasi-steady, then the aerodynamic force coefficients, normalized by instantaneous plate-LE speed, would also be constant throughout this time. In Fig. 8, force coefficient history during the phase of motion where the plate rests against its limiter shows slight oscillations superimposed on a linear trend with negative slope. That this slope is not zero, is a departure from quasi-steady response. That the slope is not large, on the contrary, vindicates the quasi-steady approximation. There is a slight trend of increasingly negative slope of force coefficients as semi-stroke to chord ratio increases. This should be viewed relative to the observations from flow visualization: smaller semi-stroke to chord ratios result in more coherent TE and LE vortices. We conjecture that these vortices do not exacerbate departure from the

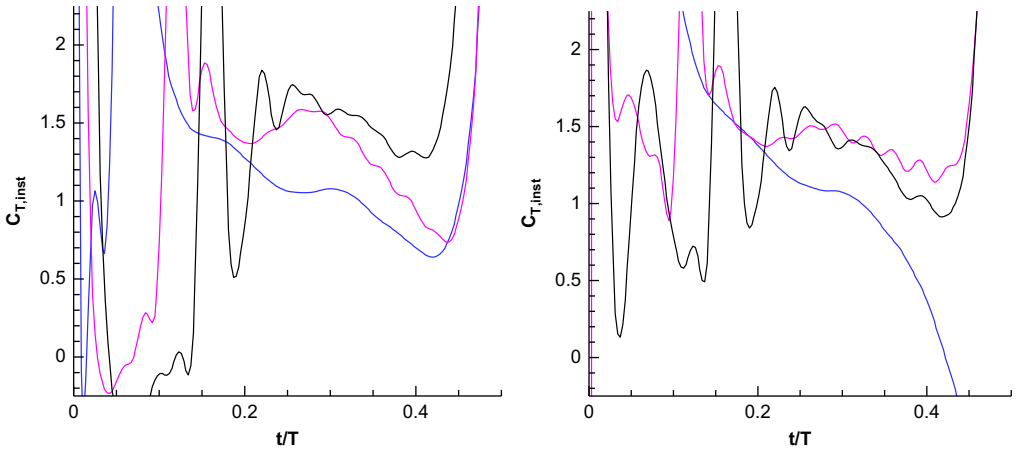

Fig. 8. Thrust coefficient (left) and normal-force coefficient (right) normalized by instantaneous LE translational speed for the aspect ratio 5.5 plate at Re=20 000; blue $h_0=6.2$, $f=0.211$ Hz; purple $h_0=3.1$, $f=0.422$ Hz; black $h_0=1.55$, $f=0.844$ Hz. Left—thrust coefficient. Right—normal force coefficient. (For interpretation of the references to color in this figure legend, the reader is referred to the web version of this article.)

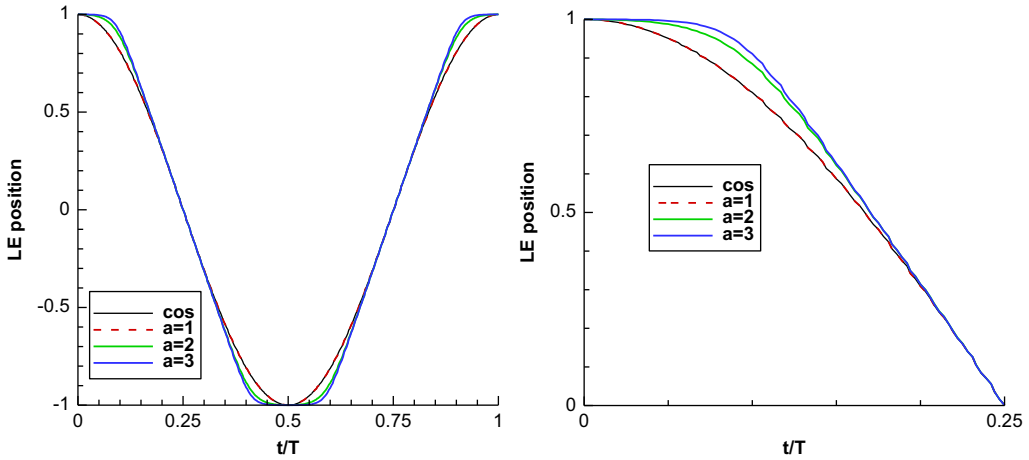

Fig. 9. Imposed kinematics of plate leading edge: sinusoidal ("cos"), and smoothings of trapezoidal, $a=1$ (coincides with sinusoidal), $a=2$ and $a=3$. Full motion history (left) and detail of $0<t/T<0.25$ (right). Ordinate normalized by amplitude of motion.

quasi-steady approximation. On the contrary, comparison of flow visualization in Figs. 5 and 6, with aerodynamic force coefficient history in Fig. 8, suggests that early in the translational portion of the semi-stroke, where the trailing-edge vortex remains close to the plate's trailing edge, thrust-coefficient and normal-force coefficient are fairly constant. As the trailing edge vortex (TEV) convects further downstream in the plate's frame of reference, there is a decline in both thrust and normal-force. For longer semi-stroke to chord ratios, the TEV has traveled a larger number of chords away from the plane, during the translational portion of each semi-stroke. It is this longer travel time which we associate with loss of suction on the plate's retreating side, and concomitant departure from quasi-steady aerodynamic response.

3.4. Sinusoidal vs. nonsinusoidal translational motion profiles

In the imposed sinusoidal motion of the plate's leading edge, there is always nonzero acceleration, with possible implications for promoting stabilization of the LEV. Acceleration produces a time-varying pressure gradient, and therefore a mechanism for continuous feeding of new vorticity into the LEV. The complementary case is a sharper acceleration of the plate's leading edge, at a small duty cycle, followed by a run of constant speed through most of the remaining semi-stroke, and a similarly sharp translational deceleration towards semi-stroke conclusion. The operative conjecture is that during the constant-speed run, there is not a clear mechanism for feeding new vorticity into the LEV, affecting LEV stability and therefore the history of aerodynamic forces. To investigate this, we constructed a set of smoothed motions resembling "trapezoidal" profiles of plate leading-edge translational history, with linear runs tangent to the sinusoidal motion, to preserve the respective peak translation speed. That is, the position of the plate's leading edge changes linearly with time, except for "corners" of the trapezoid, where the motion is smoothed. Fig. 9 shows the four cases under consideration, with the nonsinusoidal cases defined via a C^{∞} rational-function, $\hat{G}(t/T)$, proposed by Eldredge et al. (2010), and written in a form

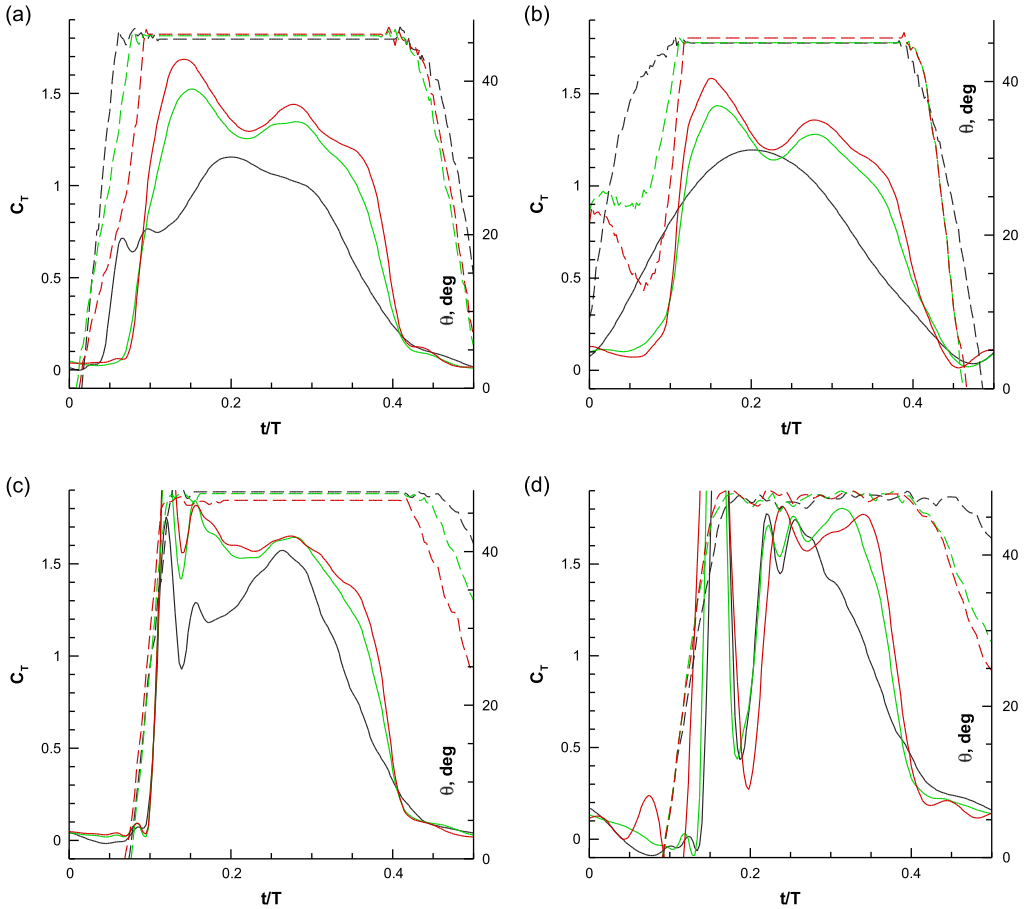

Fig. 10. Comparison of thrust coefficient for sinusoidal (a∼1 black) and nonsinusoidal (a=2 green and 3 red) motions for several AR=5.5 plate cases. Solid lines—thrust coefficient; broken lines—plate angle. (a) h_0=6.2, f=0.211 Hz, Re=20 000. (b) h_0=6.2, f=0.1055 Hz, Re=10 000. (c) h_0=3.1, f=0.422 Hz, Re=10 000. (d) h_0=1.55, f=0.844 Hz, Re=10 000. (For interpretation of the references to color in this figure legend, the reader is referred to the web version of this article.)

useful for a hovering flat plate in the sequence of expressions in Eq. (1).

$$
\begin{aligned}
G(t/T) &= ln\left[(cosh(A)cosh(D))/cosh(B)cosh(C)\right],\\
A &= 2a\left(\frac{2\pi t}{T}+\frac{2-\pi}{2}\right),\\
B &= 2a\left(\frac{2\pi t}{T}-\frac{2+\pi}{2}\right),\\
C &= 2a\left(\frac{2\pi t}{T}+\frac{2-3\pi}{2}\right),\\
D &= 2a\left(\frac{2\pi t}{T}-\frac{2+3\pi}{2}\right),\\
\hat{G}(t/T) &= h_0(1-2G(t/T)/\max(G)),
\end{aligned}
\tag{1}
$$

the function $G(t/T)$ has four non-dimensional-time parameters (A, B, C and D in Eq. (1)), one each at the "corner" of the trapezoidal motion profile. Normalized by its own maximum and multiplied by the desired translation amplitude, the result is the motion profiles in Fig. 9. The parameter "a", which controls the amount of smoothing (Fig. 9), is a dimensionless acceleration upper bound, which is limited by the capability of the motion rig to accelerate the relatively heavy horizontal carriage holding the model support (that is, overheating of the linear motors). As shown in Fig. 9, $a=1$ is nearly coincident with the sinusoidal motion, whence we consider the three cases of sinusoid, $a=2$ and $a=3$. The $a=2$ case reaches steady speed at $t/T\sim0.15$, and $a=3$ at $t/T\sim0.1$.

The first question is the extent to which the different acceleration profiles affect the rotational kinematics of the plate; that is, how is the phasing of rotation with respect to translation affected, and in particular, when does the plate attain its incidence limiter. This comparison is developed in Fig. 10, invoking symmetry to focus only on the first semi-stroke, $0\le t/T\le0.5$. For the highest-amplitude and lowest frequency case, $6.2c$ at 0.1055 Hz, the plate's rotational history is considerably affected by choice of

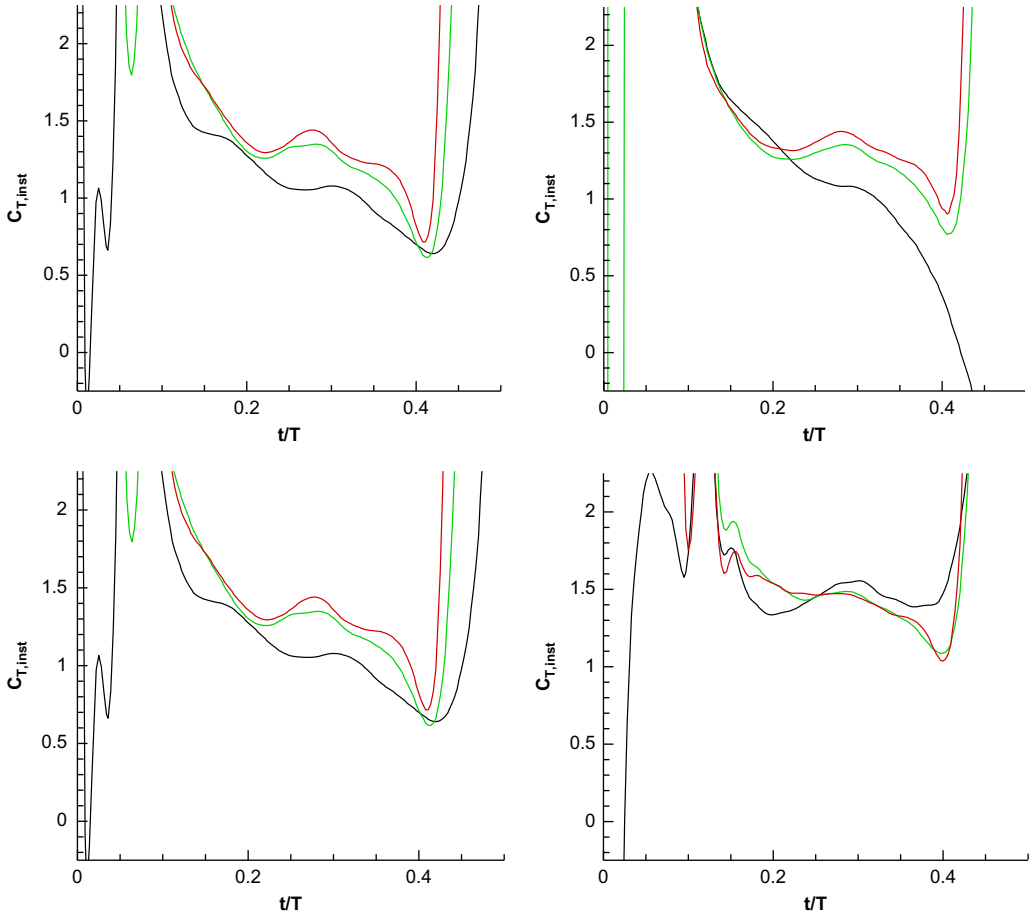

Fig. 11. Comparison of thrust coefficient (left column) and normal force coefficient (right column) for $h_0=6.2c$ and Re=20 000 (top row); and $h_0=3.1c$ and Re=10 000 (bottom row), both at $f=0.211$ Hz. Sinusoidal ($a\sim1$) and nonsinusoidal ($a=2$ and 3) velocity profiles are compared. Coefficients normalized by instantaneous speed. Line colors: black $a\sim1$; green $a=2$; red $a=3$. (For interpretation of the references to color in this figure legend, the reader is referred to the web version of this article.)

a-parameter at the semi-stroke onset (t/T~0), but the phase of the limiter-attainment event (at t/T~0.1) is unaffected, and rotational history towards semi-stroke conclusion ($t/T > 0.4$) is also similar. Evidently, slight changes in imposed LE kinematics produce material changes in dynamic pressure at semi-stroke extrema, affecting the plate's rotation at semi-stroke onset. Inversely, for the same amplitude but higher frequency, the form of the plate's rotational history as a function of phase is unaffected by choice of a-parameter, either at semi-stroke onset or conclusion, but there is a t/T~0.05 scatter in the phase position of the limiter-attainment event. For lower amplitudes and higher frequencies, the plate's rotational history at stroke onset is essentially invariant with a, but the rotational kinematics at semi-stroke conclusion have an a-dependency. This is seen for the 3.1c and 1.55c cases shown in Fig. 10.

The next question is what happens to the loads spike associable with the plate attaining its incidence limiter. As expected from the foregoing discussion, the loads spike for each respective value of semi-stroke amplitude and frequency is essentially independent of a whenever the plate's rotational kinematics appears to be independent of a for low t/T. This is evident for the 3.1c and 1.55c cases in Fig. 10. But for the 6.2c case, the difference in rotational kinematics across the various a-choices results in quite different loads history. On the other hand, differences in rotational kinematics near the semi-stroke endpoint, for t/T~0.4–0.5, do not appear to affect the aerodynamic loads.

Perhaps the most important question from the viewpoint of flapping-wing flier design is how the difference in acceleration profile affects the aerodynamic loads history during the translational portion of each semi-stroke; that is, in the time after the rotational transients have died down, and before the onset of the rotation by the start of the next semi-stroke. In Fig. 11 we again plot the aerodynamic force coefficients normalized by instantaneous speed of the plate's leading edge, for 6.2c and 3.1c semi-stroke amplitude, and 0.211 Hz frequency. Now the difference between the sinusoidal-motion and nonsinusoidal-motion respective force histories is quite attenuated, especially for the 3.1c case. Again it is worth mentioning that if the aerodynamic response were to be strictly quasi-steady, then the aerodynamic force coefficients in the instantaneous-speed normalization should be constant whenever the plate is not rotating. This is not the case; there are oscillations and a generally negative slope of force coefficient vs. t/T, in the range of $0.15 < t/T < 0.4$. But the similarity of force coefficients for the $a=1$, $a=2$ and $a=3$ motions implies that the departure from quasi-steady response is qualitatively not extreme, and is reasonably independent of rotation history. That is, the aerodynamic response to events occurring during the rotational portion of the semi-stroke does not appear to extensively propagate into the translational portion.

The motivation for considering sinusoidal vs. nonsinusoidal motion of the plate's leading edge is to assess whether imposed translational acceleration leads to stronger LEV stability and to its putative consequence, which would be a longer run of high thrust coefficient. In terms of thrust coefficient, Fig. 11 implies that broadly the answer is in the negative. The $a=1$ case has a slightly smaller decline in thrust with increasing t/T during the translational portion of the semi-stroke for the 3.1c case, and quite the opposite for the 6.2c case. One can speculate that for flapping-wing fliers, if the semi-stroke to chord ratio is not too large, then a sharp acceleration near semi-stroke extrema produces higher thrust coefficient when normalized by instantaneous flapping speed. But this is something of a moot point, as the real benefit of aggressive acceleration over a small duty cycle at each semi-stroke extremum is to have higher dynamic pressure (due to more rapidly reaching the stroke-maximum flapping speed) over a larger duty cycle.

We next revisit consideration of the loads-spike at the conclusion of the rotational portion of the semi-stroke, by comparing the freely-hinged plate with the fused-hinge plate having an approximately equivalent imposed rotation.

3.5. Prescribed-incidence histories

Fig. 12 compares results for the AR=5.5 plate between the freely-hinged and the fused-hinge versions. In the latter, the θ (t/T) variation is achieved by using all three linear motors in concert, rotating the plate's mounting strut across a $\pm 45^\circ$ range.

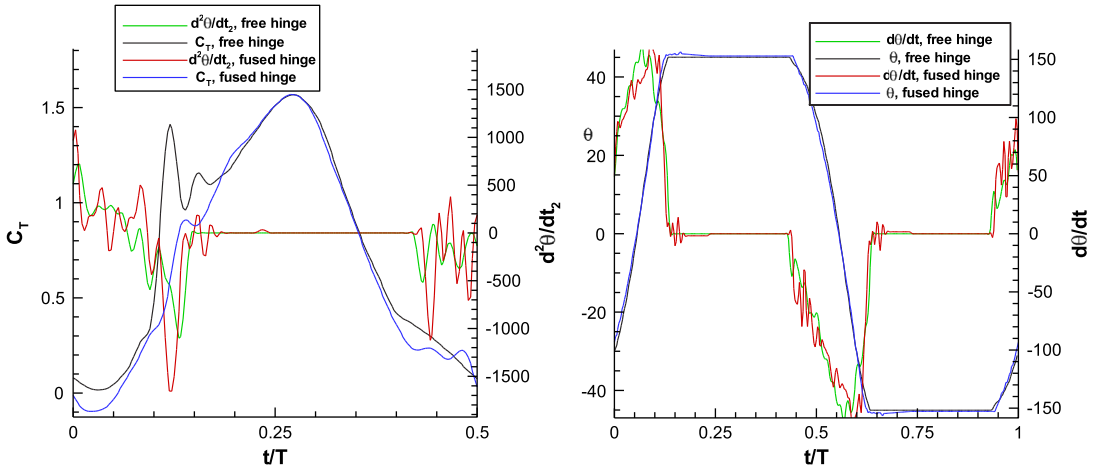

Fig. 12. Comparison of freely-hinged and fused-hinge AR=5.5 plate, 3.1c semi-stroke, 0.211 Hz frequency. Thrust coefficient and rotational acceleration vs. t/T (left), and incidence angle and rotational speed vs. t/T (right).

The left-hand portion of Fig. 12 compares thrust coefficient history with that of rotational acceleration (second derivative of $\theta(t/T)$); it is clear that the thrust-coefficient spike occurs in the t/T range where rotational acceleration is highest, but because of noise there is not a clear single rotational-acceleration peak. For the freely-hinged plate, the spike in thrust coefficient is much stronger than for the fused-hinge plate.

The incidence angle history of the fused-hinge and freely-hinged cases (right-hand portion of Fig. 12) is very similar, except for a small overshoot in maximum incidence due to elasticity in the hinge limiters (right-hand portion of Fig. 12). However, taking derivatives of position history with respect to t/T, reveals larger differences with increasing order of differentiation. Rotational acceleration history (left-hand portion of Fig. 12) differs between the two cases chiefly in the freely-hinged plate's oscillations as it impacts its incidence-limiter, and jitter in the fused-hinge plate as the trio of linear motors undergo large accelerations to flip the plate over. In the fused-hinge case, the plate does not strike against its incidence limiter, and its deceleration upon attaining its incidence maximum is instead limited by the operation of the rig. Thus one finds that the thrust coefficient histories for the fused-hinge and freely-hinged plates differ almost exclusively in the t/T increment corresponding to this portion of the rotational phase. Although measurement accuracy is insufficient to discern whether this thrust-coefficient spike is due to noncirculatory aerodynamic loads as the plate completes its rotation, or to the mechanical impact between the plate and its incidence limiter. It is however evident that the thrust coefficient spike is not due to rotational accelerations during the bulk of the plate's rotational history.

3.6. Thrust and mechanical power efficiency variations with semi-stroke to chord ratio

At least qualitatively, the thrust and normal-force behavior vary little in going from 6.2 to 1.55 semi-stroke to chord ratio. This result is consistent with the observations of Wang et al. (2004). Fig. 13 illustrates what happens to C_T as semi-stroke to chord ratio decreases: the rotational spike strengthens before reaches the extreme case of 0.3875 semi-stroke to chord ratio; the area under the curve (that is, stroke-averaged thrust) remains fairly constant until after the 1.55c case, and then declines sharply; and the rotational event occurs later and later in the semi-stroke history. Parameter studies presented above exhibit a near-symmetry between thrust and normal force; the two nearly match each other for $0<t/T<0.5$, and are anti-symmetric for $0.5<t/T<1$, due to the sign convention. For the translational portion of the semi-stroke, close agreement between thrust and normal force means that the net aerodynamic force vector is normal to the plane of the plate, since the plate is nearly at 45° incidence with respect to its local inflow. Leading edge suction is completely lost. But the right-hand plot in Fig. 13 shows the breaking of this symmetry at low semi-stroke amplitudes. For 0.775c, the two force components are still reasonably comparable during the translational portion of the semi-stroke, but the duty cycle of the translational portion is progressively lower with decreasing semi-stroke amplitude. For 0.3875c, the two force components are distinctly different.

Perhaps the most intuitively cogent scheme for assessing thrust-production efficiency of the various plate motions is the 'Figure of Merit', M, adapted from actuator disk theory; see for example (McCormick, 1995). Integrating the time-history of $C_T(t/T)$ over the stroke, and $C_N(t/T)$ multiplied by the instantaneous plate LE speed over the stroke, one obtains the stroke-averaged thrust coefficient and power coefficient, respectively:

$$C_{T,ave}=\frac{2\overline{T}}{\rho U_{ref}^2 A_{ref}}=\int_0^1 C_T\left(\frac{t}{T}\right)d\left(\frac{t}{T}\right)\ \text{and}\ C_{P,ave}=\frac{2P}{\rho U_{ref}^3 A_{ref}}=\int_0^1 C_N\left(\frac{t}{T}\right)sin\left(\frac{2\pi t}{T}\right)d\left(\frac{t}{T}\right), \tag{2}$$

where sinusoidal leading edge motion has been assumed.

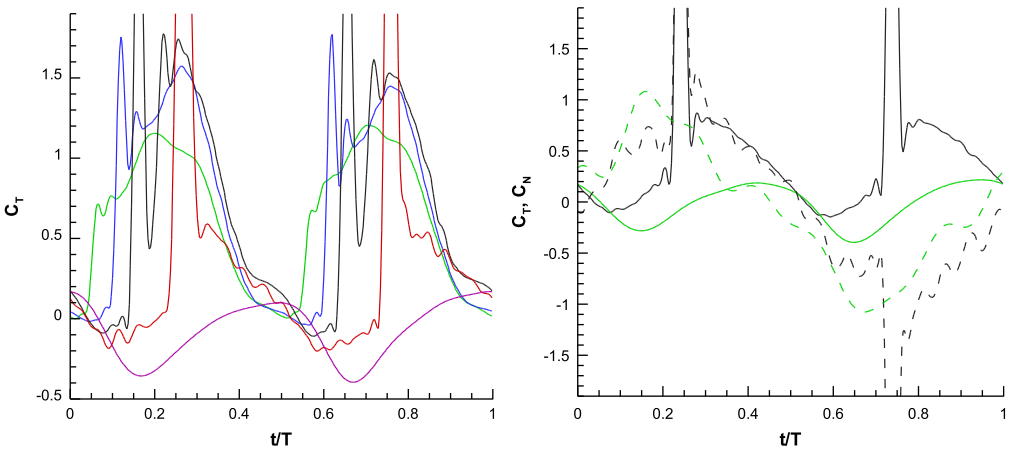

Fig. 13. Trends in aerodynamic force coefficients vs. semi-stroke to chord ratio. Left: thrust coefficient for $h_0=6.2$ (green), 3.1 (blue), 1.55 (black), 0.775 (red) and 0.3875 (purple); Re=20 000 except for $h_0=0.3875$ (purple) which is at Re=13 000. Right: thrust and normal force coefficients for $h_0=0.775$ (black) and 0.3875 (green) cases; Re=10 000. The latter illustrates "symmetry breaking" between thrust and normal force, as stroke amplitude decreases. (For interpretation of the references to color in this figure legend, the reader is referred to the web version of this article.)

In the expression for power coefficient, the dimensionless speed is $\sin(2\pi t/T)$, as units of frequency cancel out. The ideal power for producing a stroke-averaged thrust, $\overline{T}$, in hover is the usual expression from actuator disk theory,

$$P_{ideal} = \frac{\overline{T}^{2/3}}{(2\rho A)^{1/2}}, \tag{3}$$

where A is the disk (swept) area, and ρ is the fluid density (McCormick, 1995). The Figure of Merit is the ratio of ideal power to actual power:

$$M = \frac{P_{ideal}}{P} = \frac{\overline{T}^{2/3}}{P(2\rho A)^{1/2}}, \tag{4}$$

in terms of stroke-averaged thrust and power coefficients, this becomes:

$$M = \frac{C_{T,ave}^{2/3}}{2C_{P,ave}(A/A_{ref})^{1/2}}, \tag{5}$$

finally, substituting a swept area of $A=2h_0bc$ and a reference area of $A_{ref}=bc$, we obtain a definition of Figure of Merit suitable for the oscillatory motion of a flat plate:

$$M = \frac{C_{T,ave}^{2/3}}{2C_{P,ave}(2h_0)^{1/2}}. \tag{6}$$

Fig. 14 examines trends in Figure of Merit for the various plate aspect ratios, oscillation frequencies, semi-stroke to chord ratios, and freely-hinged vs. fused-hinge cases. The highest semi-stroke to chord case, 6.2c, evinces the lowest apparent value of M, clustering around the range of 0.13. Motions of 3.1 chords semi-stroke cluster around M~0.2, and 1.55c amplitude achieves the highest M, ~0.26. Further reduction in semi-stroke to chord ratio results in loss of thrust efficiency. For 0.775c, M~0.23. Not shown are the 0.3875c cases, which produce zero stroke-averaged net thrust, within the measurement margin of error. For this motion amplitude, the plate never attains its incidence angle limiters, and the combined motion of rotation and translation resembles a pure-pitching motion about the plate's midchord. The symmetry of motion intuitively implies symmetry of vertical force production in the stroke-averaged sense, and therefore zero net thrust.

The right-hand portion of Fig. 14 also compares the various translational acceleration profiles for the AR=5.5 plate leading edge: sinusoidal, and trapezoidal motions of progressively sharper corners, $a=2$ and $a=3$. There is no discernible trend of M with acceleration profile. This implies that sudden accelerations at semi-stroke extrema are not any more efficient in thrust production than is the simple sinusoidal motion. Even so, a higher stroke-averaged net thrust is produced by the trapezoidal motions, as reported in Fig. 15. Scatter in Fig. 15 is from the various frequencies of motion. Comparing the sinusoidal (a~1) and nonsinusoidal ($a=2$ and $a=3$) leading-edge translational motions for the AR=5.5 plate, one finds that stroke-averaged thrust coefficient increases for increasing values of a, for all semi-stroke to chord ratios. The right-hand side of Fig. 15, comparing the three aspect ratios for the sinusoidal-translation, shows a weak dependency on aspect ratio: smaller aspect ratio produces slightly smaller stroke-averaged thrust coefficient. But this trend is subsumed by scatter due to frequency-effects, which in turn is smaller than the main trend in thrust vs. semi-stroke to chord ratio: stroke-averaged thrust increases as stroke amplitude decreases, peaking at the 1.55c case—before decreasing precipitously. From the viewpoint of engineering a flapping-wing vehicle, it is therefore apparent that a semi-stroke to chord ratio of~1.5–3 is preferable.

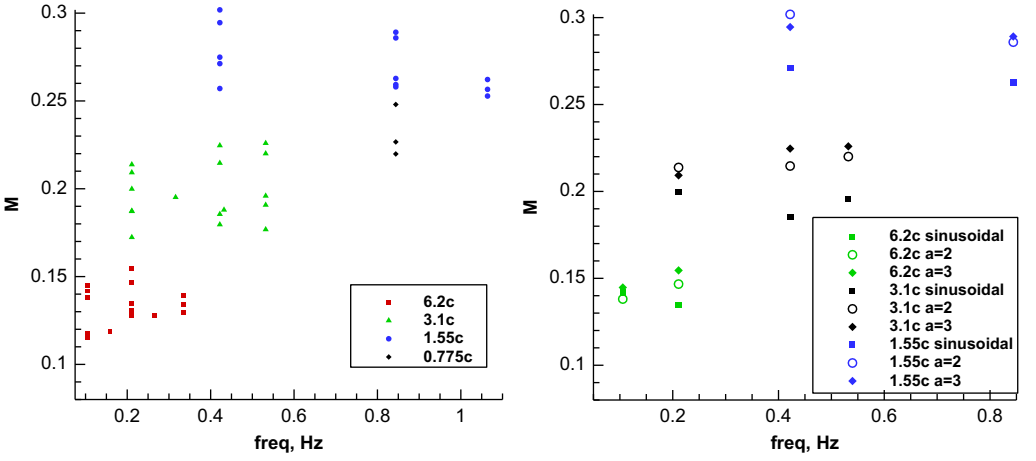

Fig. 14. Figure of Merit, M, plotted vs. frequency of oscillation (in Hz). Left: survey of results for 2D, AR=5.5 and AR=3.4 plates; right: data for AR=5.5 plate only, for sinusoidal, $a=2$ and $a=3$ motion profiles.

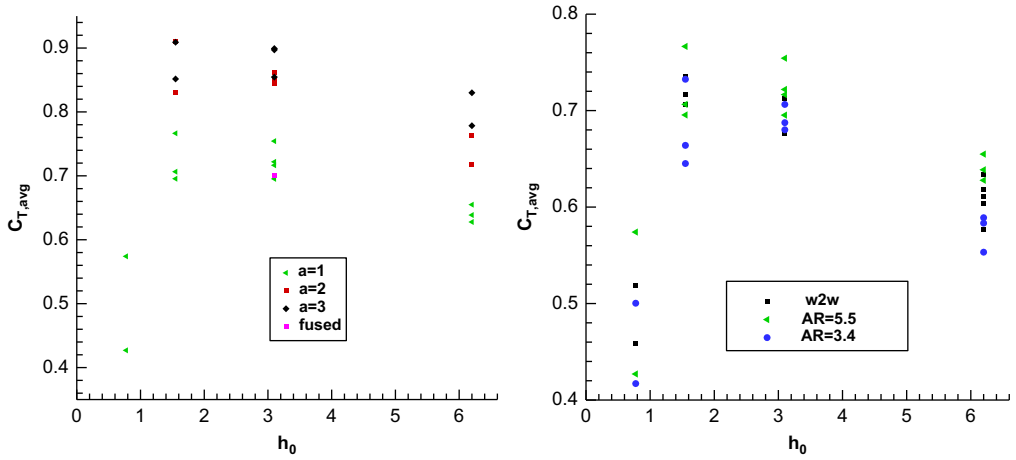

Fig. 15. Stroke-averaged thrust coefficient, vs. semi-stroke to chord ratio: comparison of sinusoidal and nonsinusoidal translational acceleration profiles for the AR=5.5 plate (left), and comparison of the three aspect ratios (2D, AR=5.5 and AR=3.4) (right).

4. Concluding remarks

Motivated by the problem of engineering abstractions of flapping-wings in hover, we revisit the classic problem of rigid flat plates undergoing periodic rotations and translations. Plates of three aspect ratios—nominally 2D, AR=5.5 and 3.4, were subjected to prescribed oscillatory fore-aft motions of their leading edge, with the plate incidence angle left to vary freely by pivoting on a hinge at the plate's leading edge, between limiters of $\pm 45^{\circ}$. Aspect ratio was seen to have essentially no effect on the history of thrust coefficient or coefficient of force opposing the motion (here termed normal-force coefficient). Reynolds number, in the range of 10 000–31 000, was also seen to have essentially no effect.

The kinematics of a plate freely hinged at its leading edge resembles the so-called delayed rotation. In no case was there evidence of wake-capture effect on aerodynamic force coefficient history. Concentrations of dye qualitatively identifiable with leading edge vortices and trailing edge vortices are produced near the semi-stroke extrema, evidently due to the rotational motion, but in sharp contrast with earlier work (Birch and Dickinson, 2003) the interaction of this vorticity with the wing does not result in a force spike at early times after stroke reversal. There is no discernible aspect ratio effect on the growth or stability of leading-edge vortices, but the 2D plate does have a more coherent vortex street in the wake underneath the plate, evidently because of more benign spanwise variations and therefore less dissipation of the dye. No evidence was found linking events in the vortex formation history with peaks in aerodynamic force coefficient. Instead, during the translational portion of each semi-stroke, the aerodynamic force coefficients, when normalized by instantaneous plate leading-edge speed, slowly decay, with faster decay for large ratios of semi-stroke to plate chord. This is strictly speaking departure from true quasi-steady aerodynamic response, but only moderately so. The fact that aerodynamic response to events occurring during the rotational portion of the semi-stroke does not appear to extensively propagate into the translational portion is further reason to regard the translational portion of the semi-stroke as quasi-steady.

Sinusoidal translation of the plate's leading edge was compared with nonsinusoidal motions, of more abrupt accelerations followed by runs of constant leading-edge translational speed. No significant difference in thrust coefficient or normal-force coefficient was found between the sinusoidal and nonsinusoidal translations. Neither was there a difference in Figure of Merit. However, the nonsinusoidal motions did produce a larger stroke-averaged thrust. Thrust production was found to have moderate dependency on semi-stroke to chord ratio: as this ratio decreases from 6.2 (the largest case examined here) to 1.55, thrust slightly increases, but further decrease in semi-stroke to chord ratio causes precipitous decline in both stroke-averaged thrust and Figure of Merit.

Acknowledgements

This investigation was sponsored by the U.S. Air Force Office of Scientific Research MURI program, Dr. D. Smith program monitor, and the U.S. Air Force Research Laboratory—University of Michigan Collaborative Center for Aerospace Sciences.

References

Birch, J., Dickinson, M., 2003. The influence of wing–wake interactions on the production of aerodynamic forces in flapping flight. Journal of Experimental Biology 206, 2257–2272.
DeVoria, A., Ringuette, M., 2012. Vortex formation and saturation for low-aspect-ratio rotating flat plate fins. Experiments in Fluids 52 (2), 441–462.
Dickinson, M., Lehmann, F.-O., Sane, S., 1999. Wing rotation and the aerodynamic basis of insect flight. Science 284, 1954–1960.
Dickson, W.B., Dickinson, M.H., 2001. The effect on advance ratio on the aerodynamics of revolving wings. Journal of Experimental Biology 207, 4269–4281.

Doman, D., Oppenheimer, M., Sigthorsson, D., 2010. Wingbeat shape modulation for a flapping-wing micro-air-vehicle control during hover. Journal of Guidance, Control and Dynamics 33 (3), 724–739.
Eldredge, J., 2007. Numerical simulation of the fluid dynamics of 2d rigid body motion with the vortex particle method. Journal of Computational Physics 221 (2), 632–648.
Eldredge, J., Toomey, J., Medina, A., 2010. On the roles of chord-wise flexibility in a flapping wing with hovering kinematics. Journal of Fluid Mechanics 659, 94–115.
Freymuth, P., 1990. Thrust generation by an airfoil in hover modes. Experiments in Fluids 9, 17–24.
Jones, A., Babinsky, H., 2011. Reynolds number effects on leading edge vortex development on a waving wing. Experiments in Fluids 51, 197–210.
Jones, A., Babinsky, H., 2010. Unsteady lift generation on rotating wings at low Reynolds numbers. Journal of Aircraft 47 (3), 1013–1021.
Kurtulus, D., David, L., Farcy, A., Alemdaroglu, N., 2006. A Parametric Stydy With Laser Sheet Visualization for Unsteady Flapping Motion. AIAA 2006-3917.
Letink, D., Dickinson, M., 2009. Rotational accelerations stabilize leading edge vortices on revolving fly wings. Journal of Experimental Biology 212, 2705–2719.
McCormick, B., 1995. Aerodynamics, Aeronautics and Flight Mechanics, second edition Wiley, pp. 291–296 (6).
Milano, M., Gharib, M., 2005. Uncovering the physics of flapping flat plates with artificial evolution. Journal of Fluid Mechanics 234, 403–409.
Ol, M.V., Bernal, L., Kang, C.-K., Shyy, W., 2009. Shallow and deep dynamic stall for flapping low Reynolds number airfoils. Experiments in Fluids 46 (5), 883–901.
Sane, S., Dickinson, M., 2002. The aerodynamic effects on wing rotation and a revised quasi-steady model of flapping flight. Journal of Experimental Biology 205, 1087–1096.
Sane, S., Dickinson, M., 2001. The control of flight force by a flapping wing: lift and drag production. Journal of Experimental Biology 204, 2607–2626.
Schouveilier, L., Hover, F.S., Triantafyllou, M.S., 2005. Performance of flapping foil propulsion. Journal of Fluids and Structures 20 (7), 949–959.
Trizila, P., Kang, C.-K., Visbal, M., Shyy, W., 2011. Low-Reynolds-number aerodynamics of a flapping rigid flat plate. AIAA Journal 49 (4), 806–823.
Vanella, M., Fitzgerald, T., Preidikman, S., Balaras, E., Balachandran, B., 2009. Influence of flexibility on the aerodynamic performance of a hovering wing. Journal of Experimental Biology 212, 95–105.
Visbal, M.R., Yilmaz, T.O., Rockwell, D., 2013. Three-dimensional vortex formation on a heaving low-aspect-ratio wing: computations and experiments. Journal of Fluids and Structures, 38, 58–76.
Wang, Z., Birch, J., Dickinson, M., 2004. Unsteady forces and flows in low Reynolds number hovering flight: two-dimensional computations vs. robotic experiments. Journal of Experimental Biology 207, 449–460.
Wood, R.J., 2007. The first takeoff of a biologically inspired at-scale robotic insect. IEEE Transactions on Robotics 24 (2), 341–347.
Yilmaz, T.O., Ol, M.V., Rockwell, D., 2010. Scaling of flow separation on a pitching low aspect ratio plate. Journal of Fluids and Structures 26 (6), 1034–1041.